PHYSICAL REVIEW APPLIED **1,** 054005 (2014)

Quantum Noise in Large-Scale Coherent Nonlinear Photonic Circuits

Charles Santori,[*] Jason S. Pelc, and Raymond G. Beausoleil
Hewlett-Packard Laboratories, 1501 Page Mill Road, MS1123, Palo Alto, California 94304, USA

Nikolas Tezak, Ryan Hamerly, and Hideo Mabuchi
Edward L. Ginzton Laboratory, Stanford University, Stanford, California 94305, USA
(Received 24 February 2014; revised manuscript received 24 May 2014; published 26 June 2014)

A semiclassical simulation approach is presented for studying quantum noise in large-scale photonic circuits incorporating an ideal Kerr nonlinearity. A circuit solver is used to generate matrices defining a set of stochastic differential equations, in which the resonator field variables represent random samplings of the Wigner quasiprobability distributions. Although the semiclassical approach involves making a large-photon-number approximation, tests on one- and two-resonator circuits indicate satisfactory agreement between the semiclassical and full-quantum simulation results in the parameter regime of interest. The semiclassical model is used to simulate random errors in a large-scale circuit that contains 88 resonators and hundreds of components in total and functions as a four-bit ripple counter. The error rate as a function of on-state photon number is examined, and it is observed that the quantum fluctuation amplitudes do not increase as signals propagate through the circuit, an important property for scalability.

DOI: 10.1103/PhysRevApplied.1.054005

I. INTRODUCTION

While all-optical logic has historically been difficult to implement [1], recent progress in micro- and nanoscale optical devices has renewed interest in this subject, as it can allow pushing energy consumption to regimes that have not been attainable in bulk optical systems. In room-temperature experiments, carrier-based optical switching has been demonstrated at 100-fJ pulse energies in silicon devices [2] and at sub-fJ pulse energies in devices made from III-V materials [3], where bistable optical memories have also been implemented [4]. Switching based on far-off-resonant (Kerr) nonlinearities typically requires higher powers but has been demonstrated at < 1 pJ in ring resonators made from amorphous silicon [5]. In low-temperature experiments, fJ-scale optical logic has been achieved in exciton-polariton systems [6], and switching near the single-photon level has been achieved in quantum dots coupled to photonic-crystal resonators [7,8]. Low-temperature atomic ensembles can also be used quite effectively for low-photon-number switching [9,10]. Thus, low-temperature switching experiments are already well into regimes where quantum effects are important for the switching dynamics [11], and room-temperature devices may soon reach such regimes, as well.

Therefore, simulation tools that can predict quantum effects in the 10–1000 photon regime are needed. Such effects include random errors due to quantum jumps, and new types of behavior that might occur when many components interact through coherent signals. Full-quantum simulation methods, such as the SLH model (the letters referring to scattering, collapse, and Hamiltonian operators) [12] and its implementation within the Quantum Hardware Description Language (QHDL) [13] may be used to study circuits containing one to three idealized components, but the exponential scaling of the state space with respect to the number of resonators requires some kind of approximation to be made before larger circuits can be studied [13–16].

Here, we describe semiclassical simulations following a method that can be applied to large-scale networks of Kerr-nonlinear resonators connected through linear optics. The stochastic differential equations we use are similar to equations used previously [17], with the dynamic field variables representing a random sampling of the Wigner quasiprobability distribution. We combine this model with a circuit solver that automatically converts a netlist, which describes an optical circuit topology, into a set of matrices representing the stochastic differential equations (see Sec. II E for a more detailed discussion of the netlist). This allows us to construct large circuits based on multiple layers of subcircuits, such as the four-bit ripple counter described below. The computation time scales polynomially with the number of components, and in many circuits, the scaling is approximately linear. Even though our model uses just one complex variable to describe each resonator, for the parameter regime of interest, we can reproduce the spontaneous switching events in one- or two-element circuits predicted by a full-quantum simulation. When the noise terms are removed, our model is the same as the coupled mode theory [18] (with energy scaled in photon units), and, thus, the same tool can be used to

---

[*] charles.santori@hp.com

perform classical simulations. Our results indicate that a pure Kerr nonlinearity combined with auxiliary coherent inputs can be used to create arbitrary logic, with tolerance to moderate linear loss, and adequate signal restoration for cascading. Such circuits can function with negligible errors at intracavity energies down to a few tens of attojoules.

II. SIMULATION METHOD

Suppose we have an optical circuit consisting of a set of nonlinear resonators connected by linear optical components, including waveguides, beam splitters, and phase shifters, and driven by coherent external inputs. When simulating such a circuit, we are interested in characterizing both its internal state as well as the resulting output fields. In modeling the internal state, we only keep track of long-lived resonator modes within the photonic structure and assume that the fields propagating in the interconnecting waveguides can always be described in terms of these resonator modes and the input fields at the same instant in time. This approximation made to simplify the computational treatment can be used for circuits with short connections between components so that the circuit dynamics occur on time scales much longer than the time it takes light to propagate across the structure. It does not allow the simulation of circuits where the propagation delays are comparable to the resonator lifetimes (typically picoseconds) or where long delay lines have been intentionally introduced (in our treatment, a delay line is just a phase shift). In the future, the ability to simulate these types of circuits can be implemented to first approximation (neglecting dispersion) by introducing delays in the differential equations.

Since we are interested in operating at fairly low light intensities, quantum shot noise can play an important role in the dynamics. Therefore, our model is of a stochastic nature: The resonator fields as well as the inputs and outputs are taken to be stochastic processes. In Sec. II A, we show how the stochastic differential equation (SDE) describing a resonator coupled to a single waveguide can be derived from a Fokker-Planck equation for the Wigner quasiprobability distribution. In Sec. II B, we extend this to multiple inputs and outputs and present the SDE that is the basis for our semiclassical model. In Sec. II C, we give the input-output relations for some static components, and in Sec. II D, we show an algebraic approach for converting a circuit containing many components into a set of SDE coupling matrices. Finally, in Sec. II E, we discuss the software and numerical implementation of our model and compare its results with those from full-quantum simulations.

A. Single-mode resonator coupled to one waveguide

We start with the simplest open-system Kerr-nonlinear resonator model featuring a single mode and a single dissipative coupling to an external field in the vacuum. This system is described by a Hamiltonian H and a single collapse operator L given by

$$H = \Delta a^\dagger a + \chi a^{\dagger 2} a^2, \tag{1}$$

$$L = \sqrt{\kappa} e^{i\psi} a, \tag{2}$$

where $a^\dagger$ and a are photon creation and annihilation operators for the resonator, L is the Lindblad-collapse operator [19] associated with photon leakage out of the resonator at a rate κ, ψ is the coupling phase, Δ is the resonator detuning from a reference frequency, and χ is the nonlinearity. The corresponding Lindblad master equation is given by

$$\dot{\rho} = -i[H,\rho] + L\rho L^\dagger - \frac{1}{2}(L^\dagger L\rho + \rho L^\dagger L) \tag{3}$$

consisting of the usual coherent part $-i[H,\rho]$ and the dissipative part $\mathcal{D}[L]\rho := L\rho L^\dagger - \frac{1}{2}[L^\dagger L\rho + \rho L^\dagger L]$.

The well-known Wigner transform of an oscillator state ρ is given by [20]

$$\mathcal{W}\{\rho\}(\alpha,\alpha^*) := \frac{1}{\pi^2}\int d^2\beta e^{-i\beta\alpha^* - i\beta^*\alpha}\mathrm{Tr}(e^{i\beta a^\dagger + i\beta^* a}\rho), \tag{4}$$

and from this we define the system's Wigner function as $W(\alpha,\alpha^*,t) := \mathcal{W}\{\rho(t)\}$. To find out how the Wigner function evolves in time, we differentiate and substitute in the master equation

$$\partial_t W(\alpha,\alpha^*,t) = \mathcal{W}\left\{\frac{d}{dt}\rho\right\} = \mathcal{W}\{-i[H,\rho]\} + \mathcal{W}\{\mathcal{D}[L]\rho\}.$$

The Wigner distribution is useful because of the correspondence between the quantum expectation values for the mode operator moments and its moments, e.g.,

$$\langle a\rangle = \langle\alpha\rangle_W, \tag{5}$$

$$\langle a^\dagger\rangle = \langle\alpha^*\rangle_W, \tag{6}$$

$$\langle n\rangle = \langle a^\dagger a\rangle = \langle\alpha^*\alpha\rangle_W - \frac{1}{2}, \tag{7}$$

$$\mathrm{Var}(n) = \langle(n - \langle n\rangle)^2\rangle = \mathrm{Var}(\alpha^*\alpha)_W - \frac{1}{4}, \tag{8}$$

$$\mathrm{Var}\left(\frac{a + a^\dagger}{2}\right) = \mathrm{Var}\left(\frac{\alpha + \alpha^*}{2}\right)_W. \tag{9}$$

This means that instead of performing a full-quantum simulation to evaluate operator expectation values, we can, instead, sample directly from the Wigner distribution.

A few calculations [17] show that

$$\mathcal{W}\{a\rho\} = \left(\alpha + \frac{\partial_{\alpha^*}}{2}\right)\mathcal{W}\{\rho\},$$
$$\mathcal{W}\{\rho a\} = \left(\alpha - \frac{\partial_{\alpha^*}}{2}\right)\mathcal{W}\{\rho\},$$
$$\mathcal{W}\{a^\dagger\rho\} = \left(\alpha^* - \frac{\partial_{\alpha}}{2}\right)\mathcal{W}\{\rho\},$$
$$\mathcal{W}\{\rho a^\dagger\} = \left(\alpha^* + \frac{\partial_{\alpha}}{2}\right)\mathcal{W}\{\rho\},$$

and these relations can be iterated to yield

$$\begin{aligned}\mathcal{W}\{[a^\dagger a,\rho]\} &= (\partial_{\alpha^*}\alpha^* - \partial_\alpha\alpha)\mathcal{W}\{\rho\},\\ \mathcal{W}\{[a^{\dagger 2}a^2,\rho]\} &= 2[\partial_{\alpha^*}(\alpha^*\alpha-1)\alpha^* - \partial_\alpha(\alpha^*\alpha-1)\alpha\\ &\quad + \frac{1}{4}\partial_\alpha^2\partial_{\alpha^*}\alpha - \frac{1}{4}\partial_{\alpha^*}^2\partial_\alpha\alpha^*]\mathcal{W}\{\rho\},\\ \mathcal{W}\{\mathcal{D}[a]\rho\} &= \frac{1}{2}[\partial_{\alpha^*}\alpha^* + \partial_\alpha\alpha + \partial_{\alpha^*}\partial_\alpha]\mathcal{W}\{\rho\},\end{aligned}$$

such that we ultimately find

$$\begin{aligned}\partial_t\mathcal{W} = &-i\Delta(\partial_{\alpha^*}\alpha^* - \partial_\alpha\alpha)\mathcal{W}\\ &- 2i\chi(\partial_{\alpha^*}(\alpha^*\alpha-1)\alpha^* - \partial_\alpha(\alpha^*\alpha-1)\alpha)\mathcal{W}\\ &- 2i\chi\left(\frac{1}{4}\partial_\alpha^2\partial_{\alpha^*}\alpha - \frac{1}{4}\partial_{\alpha^*}^2\partial_\alpha\alpha^*\right)\mathcal{W}\\ &+ \frac{\kappa}{2}(\partial_\alpha\alpha + \partial_{\alpha^*}\alpha^* + \partial_{\alpha^*}\partial_\alpha)\mathcal{W}.\end{aligned} \tag{10}$$

As discussed in Ref. [17], in order to arrive at proper Fokker-Planck equations, we must drop the third-order derivatives, i.e., the third row in Eq. (10). This is justified in the case of large photon numbers in the resonators, since, assuming $\partial_\alpha \sim 1$, the first-derivative terms containing χ are a factor of approximately $|\alpha|^2$ larger. The remaining first- and second-derivative terms can be considered as representing drift and diffusion, respectively, in a stochastic process. We can rewrite the first- and second-derivative terms of Eq. (10) as

$$\partial_t\mathcal{W} \approx -\sum_p \partial_{\alpha_p}(A_p W) + \frac{1}{2}\sum_{p,p'}\partial_{\alpha_p}\partial_{\alpha_{p'}}[(BB^T)_{p,p'}W], \tag{11}$$

where α_p with $p = \{r, i\}$ denotes the real or imaginary part of α, and

$$A_r = -\frac{\kappa}{2}\alpha_r + [\Delta + 2\chi(\alpha_r^2 + \alpha_i^2 - 1)]\alpha_i, \tag{12}$$

$$A_i = -\frac{\kappa}{2}\alpha_i - [\Delta + 2\chi(\alpha_r^2 + \alpha_i^2 - 1)]\alpha_r, \tag{13}$$

$$B_{p,p'} = \delta_{p,p'}\frac{\sqrt{\kappa}}{2}. \tag{14}$$

The stochastic equation corresponding to Eq. (11) (see Appendix B of Ref. [17]) is

$$d\alpha_p = A_p dt + \sum_{p'} B_{p,p'} dW_{p'}, \tag{15}$$

where the noise increments dW_r and dW_i are taken as independent, zero-mean, Gaussian noise processes with $\langle dW_p(t_1)dW_{p'}(t_2)\rangle = \delta_{p,p'}\delta_{t_1,t_2}dt$. Combining the above expressions, the Langevin equation for $\alpha = \alpha_r + i\alpha_i$ is

$$\begin{aligned}\dot{\alpha}(t) = &-\left\{\frac{\kappa}{2} + i\Delta + 2i\chi[\alpha^*(t)\alpha(t) - 1]\right\}\alpha(t)\\ &- \sqrt{\kappa}e^{-i\psi}\beta_{\text{in}}(t),\end{aligned} \tag{16}$$

where $\beta_{\text{in}}(t)$ is a complex Wiener process $\beta_{\text{in}}(t) = \eta^{(1)}(t) + i\eta^{(2)}(t)$, with $\langle\eta^{(m)}(t)\eta^{(n)}(t')\rangle = \frac{1}{4}\delta_{mn}\delta(t-t')$. Note that we insert a phase factor of $-e^{-i\psi}$, which has no effect on the stochastic process. However, with this phase factor, driving the resonator with an arbitrary coherent field (rather than using a vacuum state, as we have done so far) displaces $\beta_{\text{in}}(t) \to \bar{\beta}_{\text{in}}(t) + \eta(t)$, where $\bar{\beta}_{\text{in}}(t)$ is a complex-valued deterministic function of time equal to the input-field amplitude. We interpret $\beta_{\text{in}}(t)$ as representing the input field in the waveguide, which includes the quantum noise of a coherent state.

To obtain the output field in the waveguide, we can use the input-output formalism [21,22], which describes how input and output fields are related to each other and to a scattering system. For a single waveguide coupled to a system via a Heisenberg-picture coupling operator $L(t)$, the input-output relation is given as $b_{\text{out}}(t) = b_{\text{in}}(t) + L(t)$, where $b_{\text{in}}(t)$ and $b_{\text{out}}(t)$ are quantum operators representing the input and output fields in the waveguide. For our system, this leads to

$$\beta_{\text{out}}(t) = \sqrt{\kappa}e^{i\psi}\alpha(t) + \beta_{\text{in}}(t). \tag{17}$$

Alternatively, Eqs. (16) and (17) can be derived starting from the Hamiltonian of a nonlinear resonator coupled to a continuum of waveguide modes. In this picture, there are no collapse operators. One first derives a set of Fokker-Planck equations for both the resonator and waveguide modes. It is again necessary to drop the third-derivative terms associated with the Kerr nonlinearity. However, there are no second-derivative terms [17]. The input and output fields $b_{\text{in}}(t)$ and $b_{\text{out}}(t)$ are then defined as Fourier sums of the waveguide modes before and after interaction with the resonator. Since the external modes are treated from the beginning as quantum objects, the noise in $\beta_{\text{in}}(t)$ enters directly through the quantum states of the external inputs.

In this derivation, the inputs need not be coherent states, though highly nonclassical states with negative Wigner functions are still not allowed.

B. Single-mode resonators with multiple inputs and outputs

With the above work, the generalization to multiple inputs and outputs is straightforward. We, thus, assume a Hamiltonian and vector of collapse operators

$$H = \Delta a^\dagger a + \chi a^{\dagger 2} a^2, \tag{18}$$

$$\mathbf{L} = \begin{pmatrix} \sqrt{\kappa_1} e^{i\psi_1} a \\ \sqrt{\kappa_2} e^{i\psi_2} a \\ \vdots \\ \sqrt{\kappa_n} e^{i\psi_n} a \end{pmatrix}, \tag{19}$$

where we have allowed for different phases associated with each input port. Inserting these into the Lindblad master equation

$$\dot{\rho} = -i[H, \rho] + \sum_{k=1}^{n} \mathcal{D}[L_k]\rho \tag{20}$$

leads to the following SDE:

$$\dot{\alpha}(t) = -\left[\frac{\kappa}{2} + i\Delta + 2i\chi(\alpha^*\alpha - 1)\right]\alpha - \sum_j \sqrt{\kappa_j} e^{-i\psi_j} \beta_{\mathrm{in},j}(t), \tag{21}$$

$$\beta_{\mathrm{out},j}(t) = \sqrt{\kappa_j} e^{i\psi_j} \alpha(t) + \beta_{\mathrm{in},j}(t), \tag{22}$$

where $\kappa = \sum_j \kappa_k$. Equations (21) and (22) are the starting points for our semiclassical simulations. The multiple inputs and outputs can represent either waveguides or free-space modes, as needed to describe scattering loss, for example. If the input field $\beta_{\mathrm{in},j}(t)$ originates from outside the circuit, we set $\beta_{\mathrm{in},j}(t) = \bar{\beta}_{\mathrm{in},j}(t) + \eta_j(t)$, as discussed above, where $\bar{\beta}_{\mathrm{in},j}(t)$ is a deterministic coherent amplitude and $\eta_j(t) = \eta_j^{(1)}(t) + i\eta_j^{(2)}$ is a complex Gaussian noise process with zero mean $\langle \eta_j(t) \rangle = 0$ and second-order moments $\langle \eta_j^{(m)}(t) \eta_j^{(n)}(t') \rangle = \frac{1}{4}\delta_{jk}\delta_{mn}\delta(t - t')$. Alternatively, the input of one resonator may be supplied by the output of another resonator. The resulting coupled equations of motion are a system of Langevin equations, i.e., stochastic differential equations, but since the coefficients to the noise terms are state independent, they assume the same form in both the Ito and Stratonovich convention.

It is important to note that although the internal-mode variables have nonlinear equations of motion, the coupling to the external inputs and noises is fully linear. This makes it straightforward to derive rules for how to combine such systems into a circuit.

C. Static components

Besides resonators, three static components are needed: a beam splitter, a phase shifter, and a coherent displacement. These components do not have internal states; their input-output relations are fully described by a scattering matrix. For the beam splitter, which is parametrized by an angle θ:

$$\begin{bmatrix} \beta_{\mathrm{out},1}(t) \\ \beta_{\mathrm{out},2}(t) \end{bmatrix} = \begin{bmatrix} \cos\theta & -\sin\theta \\ \sin\theta & \cos\theta \end{bmatrix} \begin{bmatrix} \beta_{\mathrm{in},1}(t) \\ \beta_{\mathrm{in},2}(t) \end{bmatrix}. \tag{23}$$

A phase shifter is parametrized by a phase ϕ:

$$\beta_{\mathrm{out}} = e^{i\phi}\beta_{\mathrm{in}}. \tag{24}$$

A coherent displacement is parametrized by a displacement field β_0, which adds to the current field. This is equivalent to bouncing light off a highly reflective beam splitter with a very strong field entering through the dark port:

$$\beta_{\mathrm{out}} = \beta_{\mathrm{in}} + \beta_0. \tag{25}$$

D. Circuits of components

Stochastic equations for circuits of many components can be obtained in a straightforward, algorithmic manner. First, the input-output equations for each component $\mathcal{K}^{(i)}$ are written down in the following general form:

$$\begin{aligned} \dot{\alpha}^{(i)}(t) &= [\mathbf{A}^{(i)}\alpha^{(i)}(t) + \mathbf{a}^{(i)} + A_{\mathrm{NL}}^{(i)}(\alpha^{(i)}, t)] + \mathbf{B}^{(i)}\beta_{\mathrm{in}}^{(i)}(t), \\ \beta_{\mathrm{out}}^{(i)}(t) &= [\mathbf{C}^{(i)}\alpha^{(i)}(t) + \mathbf{c}^{(i)}] + \mathbf{D}^{(i)}\beta_{\mathrm{in}}^{(i)}(t), \end{aligned} \tag{26}$$

where i is the component index, $\alpha^{(i)}(t)$ is a vector of field amplitudes for all resonators belonging to $\mathcal{K}^{(i)}$, $\beta_{\mathrm{in}}^{(i)}(t)$ and $\beta_{\mathrm{out}}^{(i)}(t)$ are vectors of inputs and outputs to $\mathcal{K}^{(i)}$, $\mathbf{A}$, $\mathbf{B}$, $\mathbf{C}$, and $\mathbf{D}$ are constant matrices, and $\mathbf{a}$ and $\mathbf{c}$ are constant vectors. The vector $A_{\mathrm{NL}}^{(i)}$ describes the resonator nonlinearities. For static components, $\mathbf{D}$ and $\mathbf{c}$ are defined only, and the rest of the matrices and vectors are ignored because the component has no internal state.

A circuit consists of many such components $(\mathcal{K}^{(1)}, \ldots, \mathcal{K}^{(n)})$ connected together, meaning that $\beta_{\mathrm{in},m}^{(i)}(t) = \beta_{\mathrm{out},n}^{(j)}(t)$ for particular values of i, j, m, and n. A simple concatenation, in which the components connect only to external fields, obeys equations of motion of the same form (26), with the following matrices:

$$\alpha = \begin{bmatrix} \alpha^{(1)} \\ \vdots \\ \alpha^{(n)} \end{bmatrix}, \qquad A_{\mathrm{NL}}(z,t) = \begin{bmatrix} A_{\mathrm{NL}}^{(1)}(\alpha^{(1)},t) \\ \vdots \\ A_{\mathrm{NL}}^{(n)}(\alpha^{(n)},t) \end{bmatrix},$$

$$\mathbf{A} = \begin{bmatrix} \mathbf{A}^{(1)} & 0 & 0 \\ 0 & \ddots & 0 \\ 0 & 0 & \mathbf{A}^{(\mathbf{n})} \end{bmatrix}, \qquad \mathbf{a} = \begin{bmatrix} \mathbf{a}^{(1)} \\ \vdots \\ \mathbf{a}^{(\mathbf{n})} \end{bmatrix}, \qquad \mathbf{B} = \begin{bmatrix} \mathbf{B}^{(1)} & 0 & 0 \\ 0 & \ddots & 0 \\ 0 & 0 & \mathbf{B}^{(\mathbf{n})} \end{bmatrix},$$

$$\mathbf{C} = \begin{bmatrix} \mathbf{C}^{(1)} & 0 & 0 \\ 0 & \ddots & 0 \\ 0 & 0 & \mathbf{C}^{(\mathbf{n})} \end{bmatrix}, \qquad \mathbf{c} = \begin{bmatrix} \mathbf{c}^{(1)} \\ \vdots \\ \mathbf{c}^{(\mathbf{n})} \end{bmatrix}, \qquad \mathbf{D} = \begin{bmatrix} \mathbf{D}^{(1)} & 0 & 0 \\ 0 & \ddots & 0 \\ 0 & 0 & \mathbf{D}^{(\mathbf{n})} \end{bmatrix}. \tag{27}$$

Connections between components are modeled by splitting the in and out fields into "internal" (β^I) fields and "external" (β^E) fields, as follows:

$$\beta_{\mathrm{in}} = P_{\mathrm{in}} \begin{bmatrix} \beta^E_{\mathrm{in}} \\ \beta^I_{\mathrm{in}} \end{bmatrix}, \qquad \beta_{\mathrm{out}} = P_{\mathrm{out}} \begin{bmatrix} \beta^E_{\mathrm{out}} \\ \beta^I_{\mathrm{out}} \end{bmatrix}, \tag{28}$$

where P_{in} and P_{out} are permutation matrices. This is illustrated with the toy circuit in Fig. 1. In this circuit, there are four components, four external fields (solid red lines), and three internal fields (dotted lines). These permutations allow **B**, **C**, and **D** to be written in block form that separates their internal behavior from their external behavior:

$$\mathbf{B}P_{\mathrm{in}} = \begin{bmatrix} \mathbf{B}^E & \mathbf{B}^I \end{bmatrix},$$
$$P^T_{\mathrm{out}}\mathbf{C} = \begin{bmatrix} \mathbf{C}^E \\ \mathbf{C}^I \end{bmatrix},$$
$$P^T_{\mathrm{out}}\mathbf{c} = \begin{bmatrix} \mathbf{c}^E \\ \mathbf{c}^I \end{bmatrix},$$
$$P^T_{\mathrm{out}}\mathbf{D}P_{\mathrm{in}} = \begin{bmatrix} \mathbf{D}^{EE} & \mathbf{D}^{EI} \\ \mathbf{D}^{IE} & \mathbf{D}^{II} \end{bmatrix}. \tag{29}$$

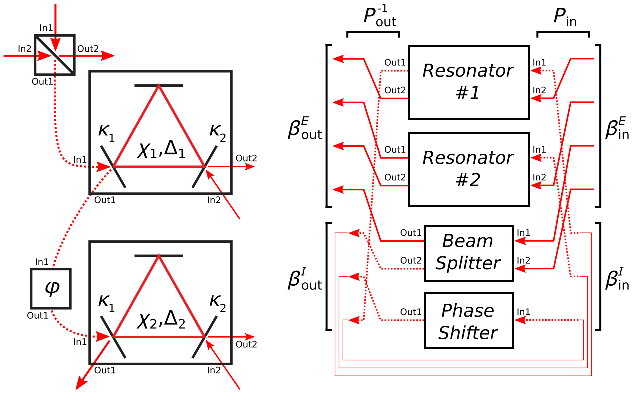

FIG. 1. Example circuit showing external ($\beta^E_{\mathrm{out}}, \beta^E_{\mathrm{in}}$) and internal ($\beta^I_{\mathrm{out}}, \beta^I_{\mathrm{in}}$) input-output fields.

The internal fields are arranged so that $\beta^I_{\mathrm{out},k}$ connects to $\beta^I_{\mathrm{in},k}$. Making these connections is equivalent to imposing $\beta^I_{\mathrm{in}} = \beta^I_{\mathrm{out}}$. One can then solve for the internal fields and eliminate them. The equations of motion for the circuit become

$$\begin{aligned} \dot{\alpha} = {} & [\mathbf{A} + \mathbf{B}^I(1-\mathbf{D}^{II})^{-1}\mathbf{C}^I]\alpha \\ & + [\mathbf{a} + \mathbf{B}^I(1-\mathbf{D}^{II})^{-1}\mathbf{c}^I] + A_{\mathrm{NL}}(\alpha) \\ & + [\mathbf{B}^E + \mathbf{B}^I(1-\mathbf{D}^{II})^{-1}\mathbf{D}^{IE}]\beta^E_{\mathrm{in}}, \end{aligned} \tag{30}$$

$$\begin{aligned} \beta^E_{\mathrm{out}} = {} & [\mathbf{C}^E + \mathbf{D}^{EI}(1-\mathbf{D}^{II})^{-1}\mathbf{C}^I]\alpha \\ & + [\mathbf{c}^E + \mathbf{D}^{EI}(1-\mathbf{D}^{II})^{-1}\mathbf{c}^I] \\ & + [\mathbf{D}^{EE} + \mathbf{D}^{EI}(1-\mathbf{D}^{II})^{-1}\mathbf{D}^{IE}]\beta^E_{\mathrm{in}}. \end{aligned} \tag{31}$$

The nonlinear part of the stochastic equations $A_{\mathrm{NL}}(\alpha)$ does not change. In other words, the only effect of interconnections is to renormalize the linear part of the input-output equations, as follows:

$$\begin{aligned} \mathbf{A} &\to [\mathbf{A} + \mathbf{B}^I(1-\mathbf{D}^{II})^{-1}\mathbf{C}^I], \\ \mathbf{a} &\to [\mathbf{a} + \mathbf{B}^I(1-\mathbf{D}^{II})^{-1}\mathbf{c}^I], \\ \mathbf{B} &\to [\mathbf{B}^E + \mathbf{B}^I(1-\mathbf{D}^{II})^{-1}\mathbf{D}^{IE}], \\ \mathbf{C} &\to [\mathbf{C}^E + \mathbf{D}^{EI}(1-\mathbf{D}^{II})^{-1}\mathbf{C}^I], \\ \mathbf{c} &\to [\mathbf{c}^E + \mathbf{D}^{EI}(1-\mathbf{D}^{II})^{-1}\mathbf{c}^I], \\ \mathbf{D} &\to [\mathbf{D}^{EE} + \mathbf{D}^{EI}(1-\mathbf{D}^{II})^{-1}\mathbf{D}^{IE}]. \end{aligned} \tag{32}$$

An alternative approach to generating the **A**, **B**, **C**, **D** coupling matrices is to propagate backwards from a given component, accumulating amplitudes from other components, splitting into additional paths when needed, and terminating at external inputs. This method works well for circuits without loops but may converge slowly if low-loss loops (effectively, cavities without internal state) are present. The algebraic approach presented above is advantageous for such loop-containing circuits, such as those in

Ref. [23]. Finally, it should be noted that instead of applying these circuit-reduction rules, one can also work in a fully quantum picture and describe the whole network using SLH models [12]. In this case, the final overall network model leads to a master equation that leads to the same SDEs as above, although, at greater computational cost, because the SLH formalism is more general and requires working explicitly with matrices whose elements are themselves noncommutative operators.

For circuits with fixed-component parameters, the coupling matrices need to be computed only once at the beginning of the simulation. The computational difficulty of integrating the SDEs scales, at worst, quadratically with the number of resonators. However, for many circuits, the coupling matrices are sparse, and the scaling is expected to be nearly linear.

E. Implementation and validity

In the remainder of this paper, we present the simulation results obtained using a model based on Eqs. (21) and (22) with $\psi_i = -\pi/2$ (this determines the rotation angle of the Wigner distribution plots). The program implemented in MATLAB allows a circuit to be defined as a netlist, which is a list of components, their parameters, and connections. In the initial implementation, the allowed components are resonators (arbitrary number of input and output ports), two-port beam splitters, phase shifters, nonoperation (identity) components, external inputs, outputs, and custom-named compound components. The compound components are similarly defined by netlists. Unless a component is an external input, a netlist entry must also specify the source of each of the component's inputs. Functions were written to flatten the netlist (by expanding compound components and connecting their inputs and outputs to the external circuit), compute circuit statistics, and check for bad connections. We initially used a back-propagation method to convert the netlist to a set of matrices **A**, **B**, **C**, **D** defining the stochastic differential equations. More recently, the algebraic approach described above has been implemented, and the two methods have been shown to produce consistent results. Integration of the stochastic equations is performed using a Euler-Maruyama time step modified to use exponential terms for the internal resonator dynamics:

$$\alpha_j[n+1] = \alpha_j[n] e^{(-i\Delta_j - \kappa_j/2 - 2i\chi_j|\alpha_j[n]|^2)\delta t} + \left(\sum_k A_{jk}\alpha_k[n] + \sum_k B_{jk}\beta_{\text{in},k}[n]\right)\delta t, \qquad (33)$$

where $\beta_{\text{in},k}[n]$ includes a deterministic time-varying drive field plus independent Gaussian random variables for each time step with amplitude $\sigma = 1/(2\sqrt{\delta t})$ for both the real and imaginary components obtained from normrnd. The time step δt is set small enough that the spontaneous jump rates in single-resonator calculations appear to be independent of δt. Typically, $\delta t = 0.025/\max(\{\Delta_j, \kappa_j\})$, which equals 5×10^{-4} for the counter circuit discussed below.

To check the validity of our semiclassical equations, we compare results with those obtained from a full-quantum simulation using the Quantum Optics Toolbox (QOT) [24]. One type of comparison is to examine the spontaneous jump rates for a single, bistable Kerr resonator with a constant drive field. As we discuss in more detail in Sec. III A below, when the drive frequency is sufficiently far detuned from the resonator, for a certain range of drive powers, the resonator can be in either of two states. In the lower-energy state, little light enters because of the large detuning. In the high-energy state, enough light has entered that the Kerr nonlinearity keeps the effective resonator frequency close to that of the input. Classically, these two states are both stable, but in the quantum regime, spontaneous jumps occur between them.

Figure 2 shows example results for a two-port resonator with $\kappa_1 = \kappa_2 = \kappa/2$ driven through one input. Figures 2(a) and 2(b) show an example with a very strong nonlinearity so that bistability occurs at very low photon numbers. Figure 2(a) shows the time-averaged behavior calculated using the steady-state density matrix solution from the QOT (black), by time averaging the solution from our semiclassical model (blue) or using the classical formula in Eq. (34) (green). Figure 2(b) shows the jump rates estimated by counting upward and downward transitions using our semiclassical model and using QOT's Monte Carlo integration. The simulation length is $t_{\max} = 1000$ time units in the QOT calculation and $t_{\max} = 10\,000$ in the semiclassical calculation. In this low-photon-number example, we see fairly good agreement in the downward jump rates r_{down}, but the upward jump rates r_{up} are quite different. This leads also to a large difference in the time-averaged photon numbers. This disagreement is not surprising given that, in its lower state, the resonator contains approximately two photons, and, thus, the approximation made in dropping the third-derivative terms from the Fokker-Planck equations (see Sec. II A) is not expected to be valid. In a somewhat higher-photon-number case [Figs. 2(c) and 2(d)], the downward and upward rates both show good, though imperfect, agreement. The semiclassical results appear to be shifted horizontally from the QOT results by $\delta\beta_{\text{in}} \sim 0.3$. For a third comparison in which the "on" state has approximately 95 photons (using $\Delta = 1.1\kappa$, $\chi = -0.3$), the jump-rate curves are again horizontally shifted by $\delta\beta_{\text{in}} \sim 0.35$ [25]. The time-averaged Wigner functions computed from the full-quantum and semiclassical simulations [Figs. 2(e) and 2(f)] look quite similar, provided that β_{in} is set to give the same ratio of upper- and lower-state populations in each case.

We also compare spontaneous jump rates in the two-resonator latch circuit presented below (Sec. III D) for the QOT and semiclassical methods. For the QOT simulation,

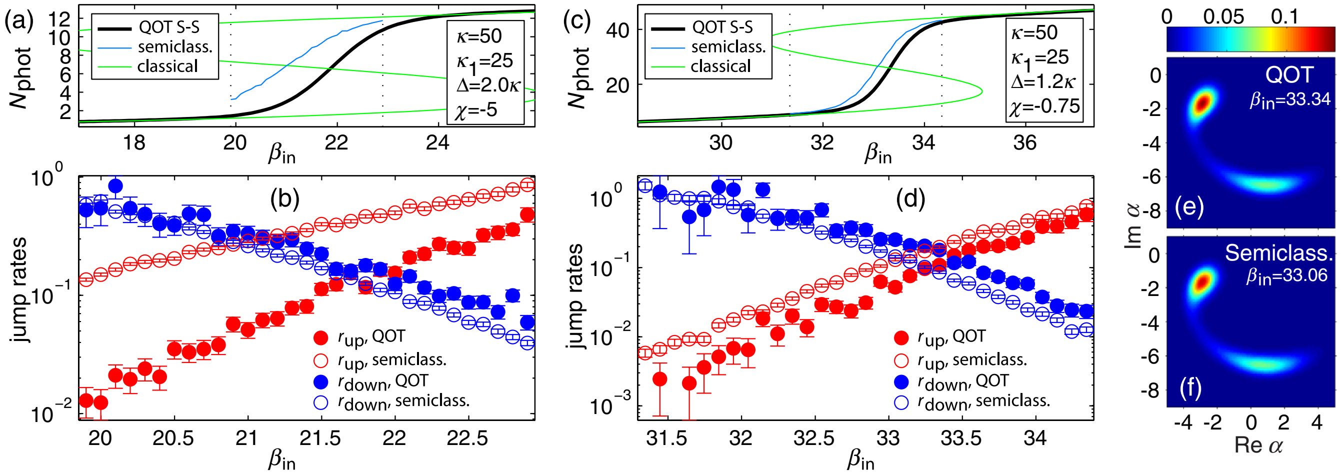

FIG. 2. (a) Time-averaged photon number vs input field $\beta_{\rm in}$ as computed using the QOT [24] steady-state solution, our semiclassical approximation, and the classical formula, in a low-photon-number regime (parameters given in figure). (b) Upward (red) and downward (blue) jump rates estimated from QOT Monte Carlo integration (solid) and semiclassical (empty circles) simulations. (c),(d) Similar to (a),(b) but in a higher-photon-number regime giving better agreement. (e),(f) Time-averaged Wigner distributions from the QOT and semiclassical simulations, with $\beta_{\rm in}$ set to obtain equal upper-and lower-state occupations; all other parameters same as in (c),(d).

we use the Hamiltonian and collapse operators given in the Supplemental Material of Ref. [26]. The results included in Fig. 10 show good agreement between the full-quantum and semiclassical methods.

Although our implementation of the semiclassical model is not optimized for speed, even for a single resonator, we see a large speed improvement compared with a full-quantum Monte Carlo simulation. This is because the semiclassical model describes the resonator with a single complex number, while the full-quantum simulation requires a number of Fock-state amplitudes that increase with increasing expected photon number. For example, for the parameters used in Fig. 2(d), simulating to $t_{\rm max} = 1000$ requires approximately 11s using a laptop computer with an Intel Core i7 processor. The corresponding QOT simulation time varies from 120 to 540 s over the range of input-field amplitudes shown in the plot. For the two-resonator latch circuit, simulating to $t_{\rm max} = 1000$ requires approximately 50 s using the semiclassical model vs 14 000 s using the QOT. For the 88-resonator counter circuit that we describe below, simulating to $t_{\rm max} = 160$ using the semiclassical model requires approximately 180 s of computation time.

III. EXAMPLES

In this section, we apply the simulation method described above to a set of optical circuits that could be of interest for switching and logic. In Sec. III A, we investigate whether circuits composed only of beam splitters, phase shifters, and resonators with an ideal Kerr nonlinearity can provide the gain and digital signal restoration needed for cascading. In Secs. III B–III E, we introduce a set of building blocks that can be used for general-purpose combinatorial and sequential logic, and as an example application, in Sec. III F, we simulate a four-bit ripple counter containing 88 resonators.

A. Inverting and noninverting amplifiers

Consider the amplifier circuit shown in Fig. 3(a). This is similar to the circuit in Ref. [26] but is simpler since it uses the signal from only one resonator output. The input field $\beta_{\rm in}$ first interferes with a constant field β_c on a beam splitter, which has amplitude transmission coefficient $\cos\theta$ and reflection coefficient $\sin\theta$ (the minus sign in the lower-left

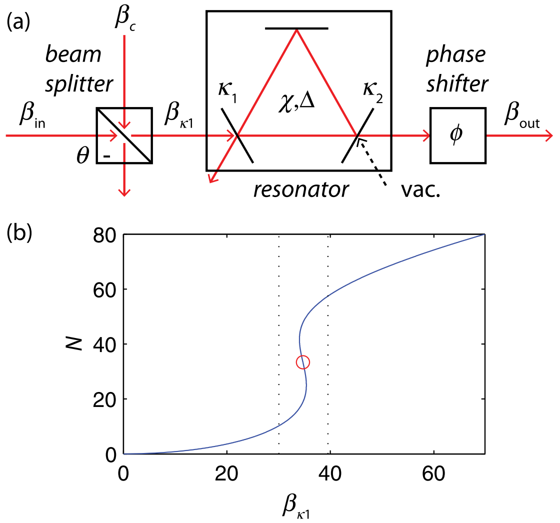

FIG. 3. (a) A simple amplifier circuit based on a nonlinear Kerr resonator. (b) Blue curve: Resonator photon number vs resonator input field in the classical approximation using the parameters from Table I. Dotted line: Designed low and high input fields. Red circle: Inflection point.

corner of the beam splitter indicates which output has a minus sign for the reflected component). The output exiting to the right is $\beta_{\kappa 1} = \beta_{\mathrm{in}} \cos\theta + \beta_c \sin\theta$. This field then enters the first input of a two-port ring resonator. In this example, we have not yet included intrinsic losses, so the total loss is the sum of the two coupling losses, $\kappa = \kappa_1 + \kappa_2$. The second resonator output passes through a phase shifter with phase ϕ that is chosen so that the output has a phase of approximately zero in the high state. This last component captures the necessity of controlling the phases between components. In an experimental realization, the phase shifter can correspond simply to a carefully chosen propagation length, or it can represent a tunable component. Whether or not active phase control is required depends on factors such as how reproducibly devices can be fabricated and the amplitude of temperature fluctuations expected during circuit operation.

This circuit can function as either a noninverting amplifier or an inverting amplifier depending on the sign of the auxiliary field β_c. Example parameters for both cases are given in Table I. Suppose, first, that we work in noninverting mode and that the design input amplitudes to stage 0 are $\beta_{\mathrm{in}} = \{0, 10\}$. Since the beam splitter is highly transmissive, it serves mainly to displace the field with little loss in amplitude so that the field incident onto the resonator is $\beta_{\kappa 1} = \{30.04, 39.53\}$. The resonator then serves as a nonlinear filter, as represented by the blue curve in Fig. 3(b), which is the steady-state solution to Eqs. (21) and (22) without the noise terms:

$$\kappa_1 |\beta_{\mathrm{in},1}|^2 \approx n[(\kappa/2)^2 + (\Delta + 2\chi n)^2], \tag{34}$$

where $\beta_{\mathrm{in},1}$ is the external field incident on one of the resonator inputs, $n \approx |\alpha|^2$ is the resonator photon number, and we have taken the limit $n \gg 1$. From this equation, one can show that classical bistability occurs for $\Delta > \frac{\sqrt{3}}{2}\kappa$, if $\chi < 0$. The red circle marks an inflection point in the rhs of the above equation, $n_{\mathrm{inflection}} = -\frac{\Delta}{3\chi}$. The parameter values used in Fig. 3(b) are given in Table I (stage 0).

TABLE I. Simulation parameters used for the four-stage noninverting and inverting amplifiers.

	Amplifier parameters			
Stage	0	1	2	3
$t = \cos\theta$	$\sqrt{0.9}$	$\sqrt{0.9}$	$\sqrt{0.9}$	$\sqrt{0.9}$
$r = \sin\theta$	$\sqrt{0.1}$	$\sqrt{0.1}$	$\sqrt{0.1}$	$\sqrt{0.1}$
χ	−0.5	−0.5	−0.5	−0.5
κ_1	25	50	100	200
κ_2	25	50	100	200
Δ	50	100	200	400
	Noninverting			
Design β_{in}	$\{0, 10\}$	$\{17, 37\}$	$\{26, 77\}$	$\{45, 145\}$
β_c	95	140	285	580
ϕ	−3.42	−3.42	−3.42	−3.42
	Inverting			
Design β_{in}	$\{0, 10\}$	$\{17, 37\}$	$\{32, 80\}$	$\{62, 163\}$
β_c	−125	−300	−607	−1215
ϕ	−0.2	−0.65	−0.74	−0.74

With these parameters, the nonlinear resonator is near the onset of bistability and exhibits a thresholdlike response. The dotted lines in Fig. 3(b) represent the designed resonator field amplitudes for "low" and "high" inputs. The field exiting the resonator on the right has amplitude approximately equal to $\sqrt{\kappa_2 n} \approx \{17, 37\}$ for low and high inputs, respectively, and, thus, the input field swing of 10 is amplified by a factor of 2. A nonideal feature of this simple circuit is that the low output is nonzero and has a different phase than that of the high output. The residual low output may cause complications when cascading components but can be eliminated by adding an interference path [26], as is included in the logic components that we introduce starting in Sec. III B.

Because of its thresholdlike behavior, this amplifier has some digital signal restoration capability. Here, we perform simulations with a linearly varying triangle-wave input, with amplitude between 0 and 10, to examine whether the signal restoration in the presence of quantum noise is sufficient for cascading. For multiple stages, since each stage receives a larger input amplitude, the parameters for each amplifier stage must be chosen differently (Table I) to match the switching thresholds with the expected low and high resonator inputs. The simulated output-field amplitudes of four cascaded inverting amplifiers are shown in Fig. 4(a). We see that, despite the badly behaved input, the first stage (blue curve) has a clear switching behavior, although there is some variation in the output amplitude within the high and low states. In subsequent stages, the curves are quite flat in between switching events, and, furthermore, the short-time-scale noise due to quantum fluctuations does not appear to increase from one stage to the next. The corresponding output phases are plotted in Fig. 4(b). The phase noise can be seen to decrease with each stage.

When performing these simulations, we notice a markedly different behavior when we cascade inverting or noninverting amplifiers. This is seen most easily in the time-averaged complex field distributions of the resonators for the two cases, which are plotted in Figs. 5 and 6. The figures use a logarithmic scale in order to cover > 4 orders of magnitude, allowing the faint connections between the high and low states to be seen. In either case, in the first amplifier stage, we see that the high state has a larger phase variation than the low state, which is a general feature for Kerr resonators even for constant inputs. In the inverting case, this noisier high state from the first stage leads to a low state in the second stage, which largely resets the noise. In the noninverting case, the high state from the first stage leads to another high state in the second stage, allowing the

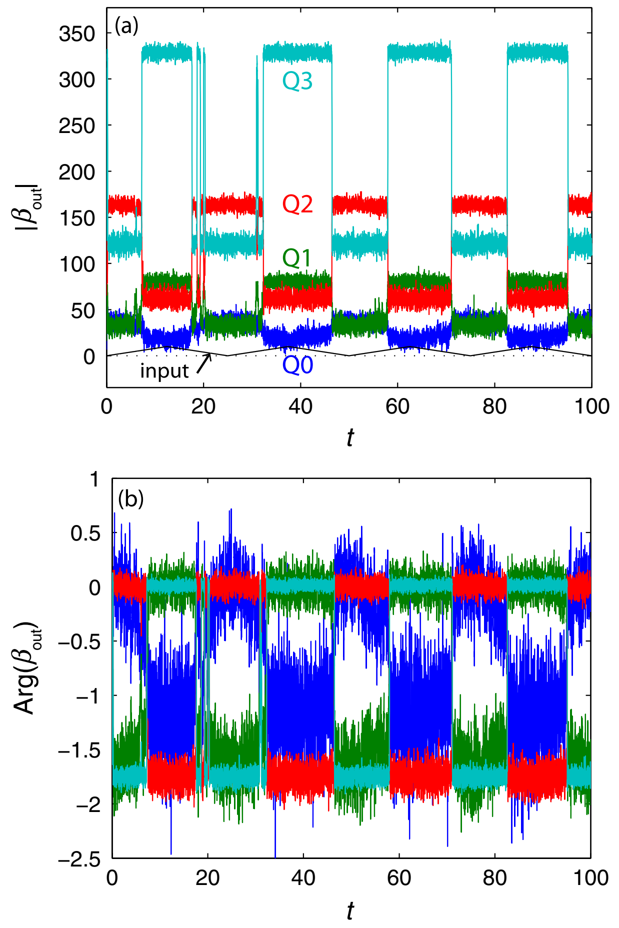

FIG. 4. (a) Simulated output amplitudes from stages 0, 1, 2, and 3 (labeled Q0, Q1, etc.) for four cascaded inverting amplifiers using a triangle-wave input (black curve) with amplitude varying linearly between 0 and 10. The fields are averaged over a time interval of 0.01. (b) Corresponding output phases.

phase noise to propagate further, even though it is diluted by the contribution of the next auxiliary coherent-state input. As a result, the phase noise in the last stage is larger for the noninverting amplifiers compared with the inverting amplifiers. If each amplifier is driven with a constant input, $\langle\beta_{\mathrm{in}}\rangle = 10$, after the fourth stage, the phase noise amplitude of the noninverting amplifier chain is 53% higher than for the inverting amplifier chain. This is part of the motivation for using inverting amplifiers in the fanout circuits that we present below.

B. AND gate

The first logic gate we consider is the AND gate shown in Fig. 7(a). This is the same circuit that is shown in Fig. 1(a) of Ref. [26], except that here we include an intrinsic resonator loss, which is unavoidable in practical photonic integrated circuits. Even if we have complete control over the resonator's output coupling rates, if we optimize for the lowest possible switching energy, then the intrinsic losses will be comparable to the coupling losses. Suppose, for example, that we design a gate to work near the onset of bistability, with $|\Delta| = \kappa$. The switching photon number will be close to the inflection point in the bistability curve,

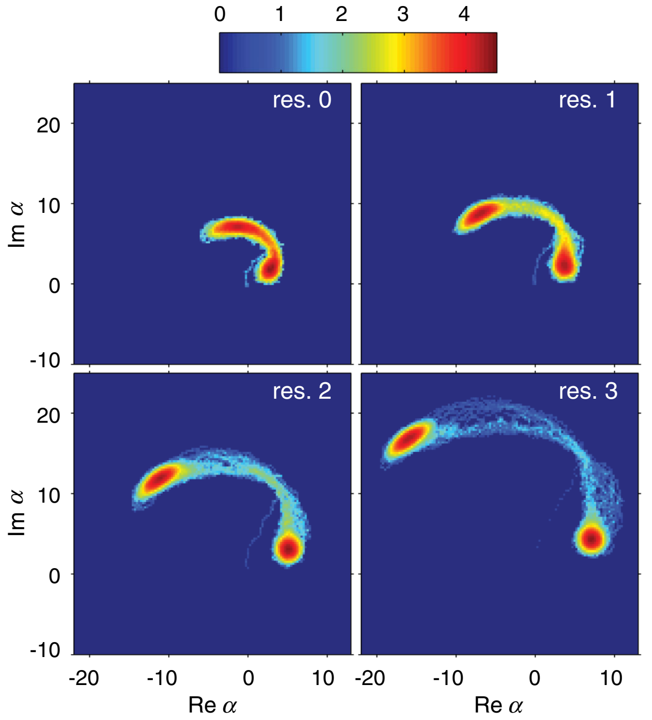

FIG. 5. Base-10 logarithm of the unnormalized, time-averaged distribution of the complex resonator fields in a four-stage inverting amplifier circuit using a triangle-wave input.

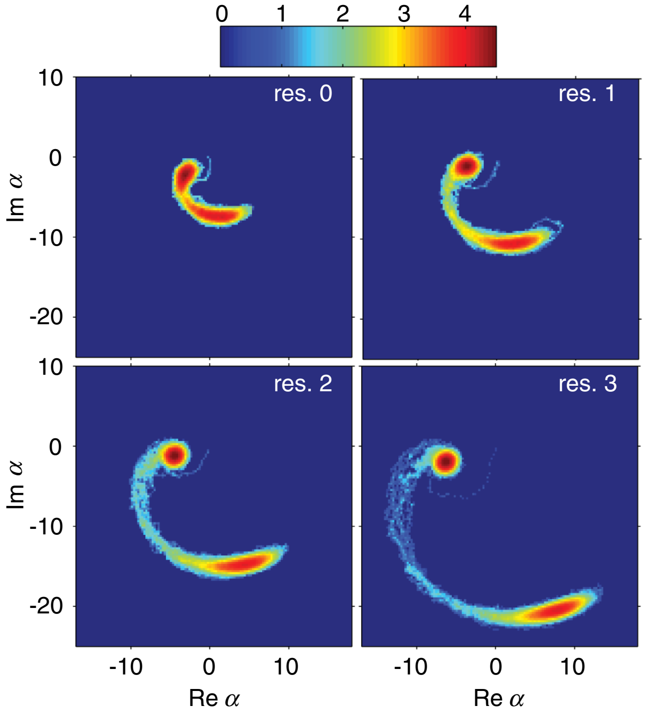

FIG. 6. Same as Fig. 5 but using noninverting amplifier stages.

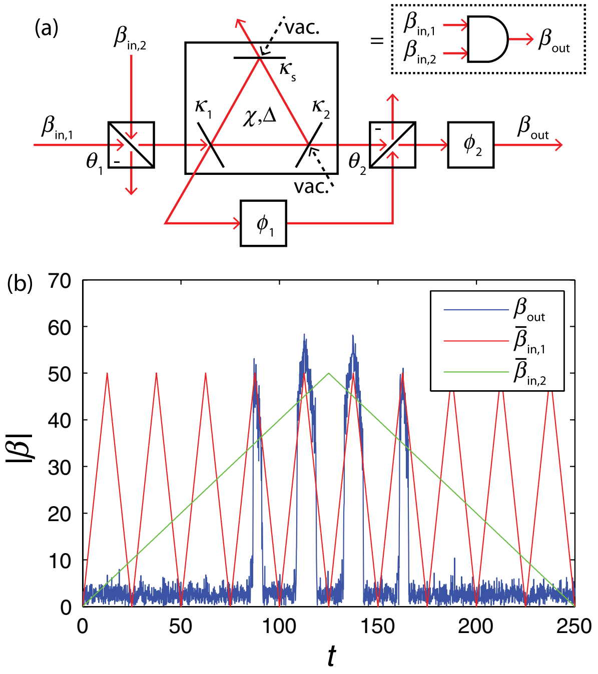

FIG. 7. (a) AND circuit based on a nonlinear Kerr resonator. (b) Simulated output field (blue) for triangle-wave inputs (red, green), with $E_{\rm high} = 50$. The fields are averaged over a time interval of 0.01.

TABLE II. Parameters for the basic circuits. Here, $E_{\rm high}$ is the high level for external inputs. The simulations use $E_{\rm high} = 50$ (resonator photon number approximately 100) or $E_{\rm high} = 20$ (resonator photon number approximately 20).

	AND	Fanout	Latch
Design $\beta_{\rm in}$	$\{0, E_{\rm high}\}$	$\{0, E_{\rm high}\}$	$\{0, E_{\rm high}\}$
β_c		$-2.6E_{\rm high}$	$1.75e^{-i\phi_1}E_{\rm high}$
χ	$-653.4/E^2_{\rm high}$	$-348.48/E^2_{\rm high}$	$-512.5/E^2_{\rm high}$
κ_1	20	20	20
κ_2	20	20	20
κ_3	10	10	10
Δ	50	50	50
$t_1 = \cos\theta_1$	0.707	0.707	0.707
$t_2 = \cos\theta_2$	0.89	0.89	0.629
$t_3 = \cos\theta_3$		0.707	0.829
ϕ_1	−1.39	−1.45	2.72
ϕ_2	2.65	−0.46	0.14
ϕ_3			2.34

$n_{\rm switch} \approx |\Delta/(3\chi)|$. Using Eq. (34) for the input field $\beta_{\rm in}$ and setting the minimum switching energy (in photon units) to be $U_{\rm switch} \approx |\beta_{\rm in}|^2/\kappa$, we find

$$U_{\rm switch} \approx \frac{\kappa^2}{|\chi|\kappa_1}. \tag{35}$$

Setting $\kappa = 2\kappa_1 + \kappa_3$, where κ_3 is the intrinsic loss and minimizing $U_{\rm switch}$ with respect to κ_1, we obtain $\kappa_3 = 2\kappa_1 = \kappa/2$ so that the intrinsic loss is half of the total loss. However, with such a large relative intrinsic loss, it is difficult to design circuits in which the output-field amplitudes are as large as the input amplitudes. Thus, we back off from the optimum and use $\kappa_3 = 0.2\kappa$. The circuit parameters that we use to simulate the AND gate are given in Table II.

The AND gate works as follows: The two inputs interfere on a 50-50 beam splitter. Only if both inputs are high (and in phase), the beam splitter output is large enough to exceed the switching threshold of the resonator. We can simply use the output from resonator mirror 2 as the final output, as we do in the amplifiers discussed above. However, the performance can be improved by taking the output from resonator mirror 1, adjusting its phase, and interfering it with the output from resonator mirror 2 on a second beam splitter. We adjust the phase ϕ_1 and the mixing angle θ_2 so that when only one of the circuit inputs is high, the signals entering the second beam splitter interfere destructively, giving a low output close to zero. The final phase shift ϕ_2 is chosen so that the high output has its phase close to zero.

Figure 7(b) shows the simulated operation of the AND gate. Triangle waves are used to drive both inputs to test the circuit's capability for digital signal restoration. The high output amplitude slightly exceeds the designed input high amplitudes. A separate simulation, in which the circuit is driven by a square-wave signal, indicates propagation delays (for the output to cross a level halfway between the steady-state low and high levels) ranging from $\tau = 0.023 = 1.2/\kappa$ for the fastest $\{1,1\} \to \{0,0\}$ input transition to $\tau = 0.091 = 4.6/\kappa$ for the slowest $\{0,1\} \to \{1,1\}$ transition. Because of the direct path from the input to the output (through ϕ_1), the output can also exhibit short spikes if the inputs transition suddenly from $\{0,0\}$ to $\{1,0\}$.

C. Inverting fanout

The AND gate described above has only a single optical output. Splitting this in two before sending it to other gates (such as more AND gates) will fail, since the amplitudes will be a factor of $1/\sqrt{2}$ smaller and will be near or below the switching thresholds of the subsequent gates. Here, we briefly introduce an inverting amplifier circuit that can be used both as a 2× fanout and as a NOT gate to complement the AND gate above, allowing for universal combinatorial logic.

Figure 8(a) shows the inverting fanout circuit, which is similar to the AND gate above, with a few differences. One of the inputs is replaced by a constant coherent drive, which has a larger amplitude and is 180° out of phase with respect to the remaining input. The resonator nonlinearity is also decreased in order to increase the switching threshold. In an integrated photonics implementation, the per-photon nonlinearity can be changed most easily by varying the resonator length. The circuit parameters are

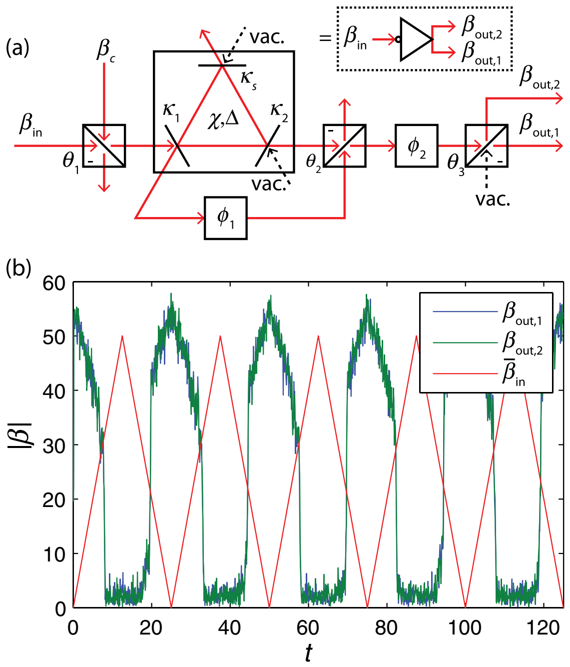

FIG. 8. (a) Inverting 2× fanout circuit based on a nonlinear Kerr resonator. (b) Simulated output fields (blue, green) for a triangle-wave input (red), with $E_{high} = 50$. The fields are averaged over a time interval of 0.01.

given in Table II. As a result of these changes, the output field in the high state has sufficient amplitude that it can be divided in two at a final 50-50 beam splitter, yielding two outputs with amplitudes slightly above the designed high level. Figure 8(b) shows the simulated behavior of this circuit for a triangle-wave input, demonstrating the digital signal restoration capability of this circuit. For a square-wave input, the propagation delays (for midlevel crossing) are $\tau = 0.105 = 5.3/\kappa$ for the upward output transition and $\tau = 0.058 = 2.9/\kappa$ for the downward transition.

If fanout to many outputs is required, one can design special circuits similar to the cascaded amplifiers that we describe in Sec. III A. However, for simplicity of the present demonstration, we limit the number of primitive components, cascading the 2× fanout as needed to create additional copies of a signal.

D. Latch

To add memory to our circuits, we start with the $\overline{SR}$-NAND latch from Ref. [26]. The main change we make to the version shown in Fig. 9(a) is to incorporate intrinsic resonator losses, which require adjusting the other parameters (see Table II) so that the resonators operate closer to their switching thresholds. We might expect this to make the circuit more sensitive to noise.

The behavior of this circuit simulated in Fig. 9(b) can be understood as follows. Let us name the upper and lower resonators in the diagram resonators 1 and 2, respectively.

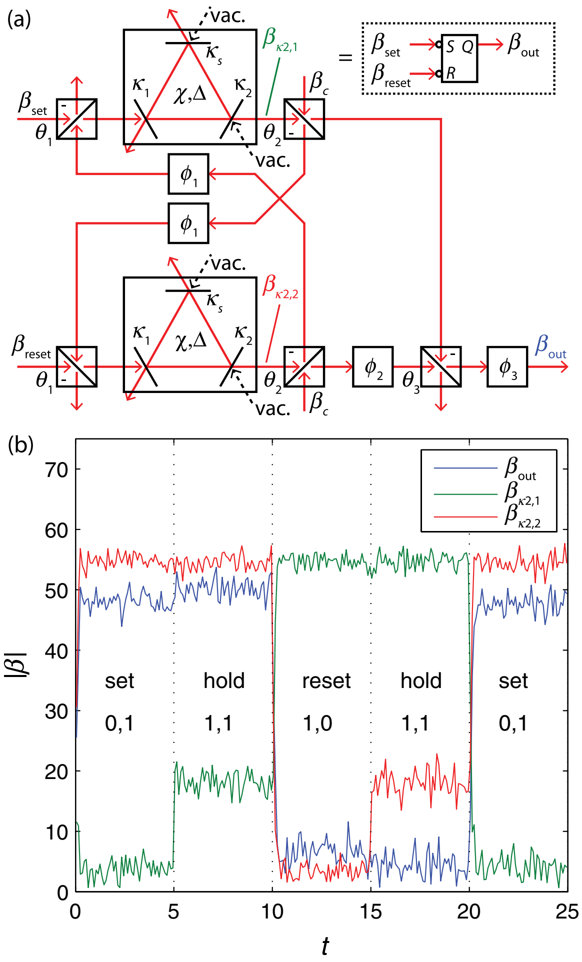

FIG. 9. (a) Latch circuit using two nonlinear Kerr resonators (see Ref. [26]). (b) Simulated final output field (blue), and the fields exiting from the κ_2 ports of resonators 1 and 2 (the upper and lower resonators in the diagram, respectively, green and red curves). For times in between the vertical lines, the two input levels are held constant at $\{0,1\}E_{high}$, as indicated, with $E_{high} = 50$. The fields are averaged over a time interval of 0.01.

If β_{reset} is high and resonator 1 is off, the coherent input β_c entering from the top of the diagram interferes constructively with β_{reset} so that the input to resonator 2 exceeds its switching threshold, keeping it in its “on” state. The feedback phase is chosen such that the κ_2 output of resonator 2, feeding back to the input of resonator 1, interferes destructively with the other inputs, keeping resonator 1 in its “off” state, independent of whether β_{set} is low (the “set” condition) or β_{set} is high (the “hold” condition). On the other hand, if β_{set} is high and β_{reset} is low (the “reset” condition), resonator 1 turns on and resonator 2 turns off. If β_{reset} then goes high again (the “hold” condition), resonator 1 stays on and resonator 2 stays off. Thus, in the hold condition, the system retains its previous state. The maximum propagation delay (for midlevel crossing) is $\tau = 0.11 = 5.5/\kappa$.

For $E_{\rm high} = 50$, resonator 1 contains approximately 0.5 photons in its undriven (set) state, 17 photons in its lower hold state, and 150 photons in its driven (reset) and higher hold states. The corresponding output-field amplitudes are $\beta_{\kappa_2,1} \approx \sqrt{\kappa_2 n} \approx \{3, 18, 55\}$. The parameters of the final beam splitter, which combines the outputs from the two resonators, and the associated phase ϕ_2, are chosen so that the final output is as close as possible to $E_{\rm high}$ whenever resonator 2 is in its high state, and as close as possible to zero, otherwise.

When $E_{\rm high} \leq 25$, spontaneous jumps between the two bistable states of the hold condition occur with sufficient frequency to allow accurate estimation of the jump rate, as shown in Fig. 10. When $E_{\rm high} \leq 15$, this rate becomes too large to allow accurate state determination in between jump events, but we extend the estimate to lower fields by fitting an exponential decay to the resonator field autocorrelation function. We should point out that, as $E_{\rm high} \to 0$, the semiclassical approximation is expected to become less and less accurate.

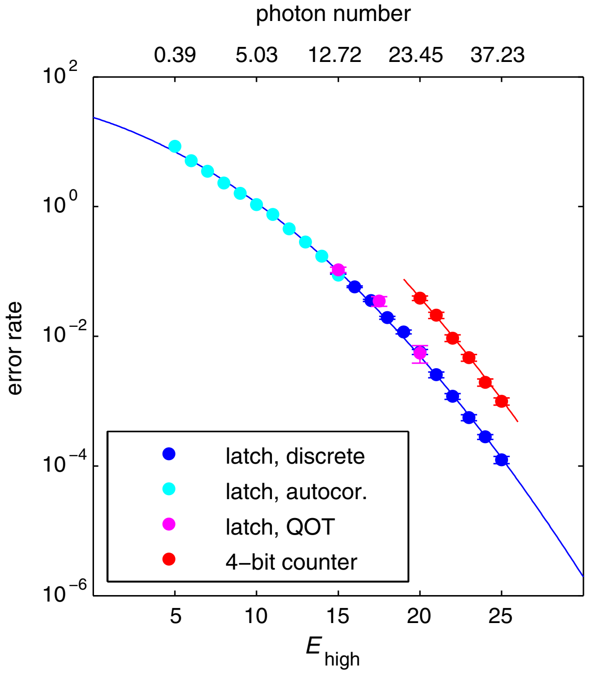

FIG. 10. Dark blue points: Simulated spontaneous jump rates for a latch circuit in the hold condition plotted as a function of the input-field amplitude $E_{\rm high}$ (other circuit parameters are tied to $E_{\rm high}$ as described in Table II). The error bars assume Poisson statistics for the number of detected jumps. Cyan points: Simulated jump rate in the low-field regime estimated by fitting an exponential decay to the resonator field autocorrelation. Blue curve: Quadratic fit to the logarithm of the jump rate. Magenta points: Results obtained using the QOT [24,26]. Red points: Simulated jump rate for the four-bit counter circuit. Red curve: Same as the blue curve but multiplied by 8 (see text). The top x axis indicates the mean photon number corresponding to $E_{\rm high}$ for a resonator in its on state during the set condition.

In solid-state implementations, our time units will likely correspond to intervals ranging from picoseconds to nanoseconds, and, thus, an acceptable error rate for computing can be estimated as $< 10^{-18}$. By fitting a quadratic polynomial to the logarithm of the jump rate and extrapolating to higher input fields, we estimate that $E_{\rm high} \approx 54$ is required to achieve this, corresponding to approximately 177 photons contained within a resonator in its on state during the set condition (this corresponds to 35 aJ at $\lambda = 1\ \mu$m).

E. Type-*D* flip-flop

We next combine the primitive components defined above to make a clocked memory component that functions the same as the *D* flip-flop in electronics [27]. The circuit schematic is shown in Fig. 11(a) (see the previous figures for gate symbol definitions). This circuit is built around two set-reset $\overline{SR}$ NAND latches denoted as "master" and "slave." The main input is denoted β_D, the clock is $\beta_{\rm clock}$, the intermediate master output is β_M, and the final slave output is β_Q. AND gates, with the clock or its compliment as one of the inputs, are used to control when the latches can change states. When the clock is high, β_D controls the state of the master latch, while the slave latch is frozen. When the clock goes low, the master latch is frozen, but its state is

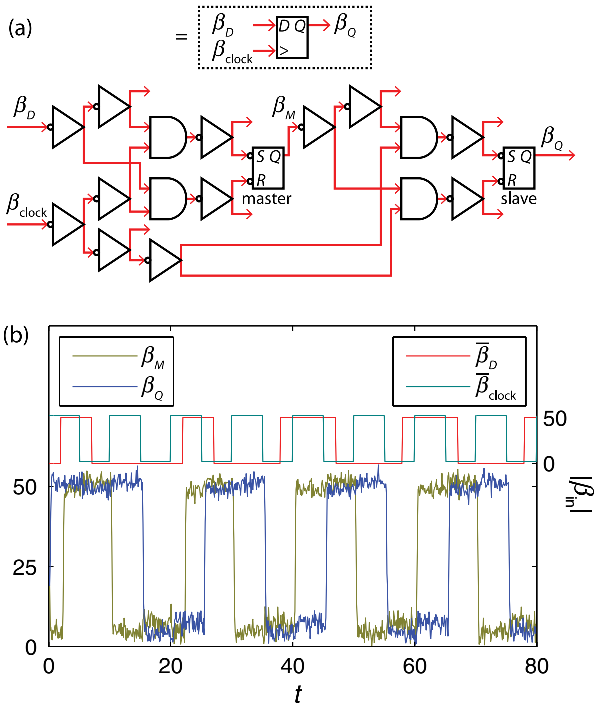

FIG. 11. (a) Schematic for a *D* flip-flop built from the primitive circuits described above. (b) Simulated master output (yellow) and final slave output (dark blue) in response to the main input (red) and clock (light blue) square-wave signals. The simulation used $E_{\rm high} = 50$, and the plotted fields are averaged over a time interval of 0.01.

transferred to the slave latch. Numerous inverting fanout gates are also required, either to divide or invert the various signals. Since these components account for more than half of the resonators in the circuit, replacing them with modified AND gates or improved amplifiers will be one of the more straightforward ways to optimize this circuit.

The simulated circuit dynamics are shown in Fig. 11(b). For the first two input pulses (red), the rising edges occur when the clock (light blue) is already high, and, thus, the master latch (yellow) switches at the input rising edge. For the second two input pulses, the rising edges occur before the clock is high, and, thus, the master latch switches at the clock rising edge. The slave latch (dark blue) always transitions at the falling clock edge. Close examination shows that propagation delays (for midlevel crossing) of up to $\tau = 0.51 = 25.5/\kappa$ can occur following clock edges. This is approximately as one would expect from summing the individual component delays given above. For the slave transition, the path from the clock to the output passes through four fanouts (with two upward and two downward transitions), an AND gate (upward), and a latch (can be upward). This circuit includes 20 resonators, 54 vacuum inputs, 16 nonvacuum coherent-state inputs, 54 beam splitters, and 40 phase shifters. It is our first example of a circuit too large to simulate using known full-quantum methods.

F. Four-bit counter

As a simple application of the D flip-flop, here we demonstrate a four-bit ripple counter. The circuit shown in Fig. 12 contains four flip-flops, each representing one of the bits. The output of each flip-flop is inverted and fed back into its main input, causing its output state to toggle at each falling clock edge. Additionally, the output of a given flip-flop serves as the clock signal of the flip-flop representing the next-higher-order bit. Thus, two inverting fanout components are required at each stage to generate the required copies.

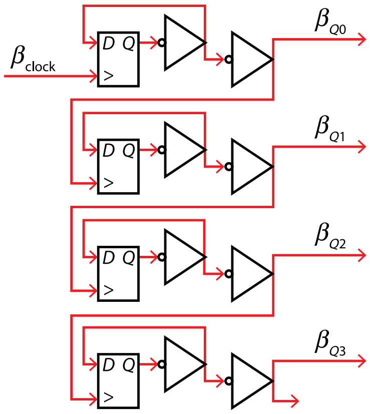

FIG. 12. Circuit diagram for a four-bit ripple counter.

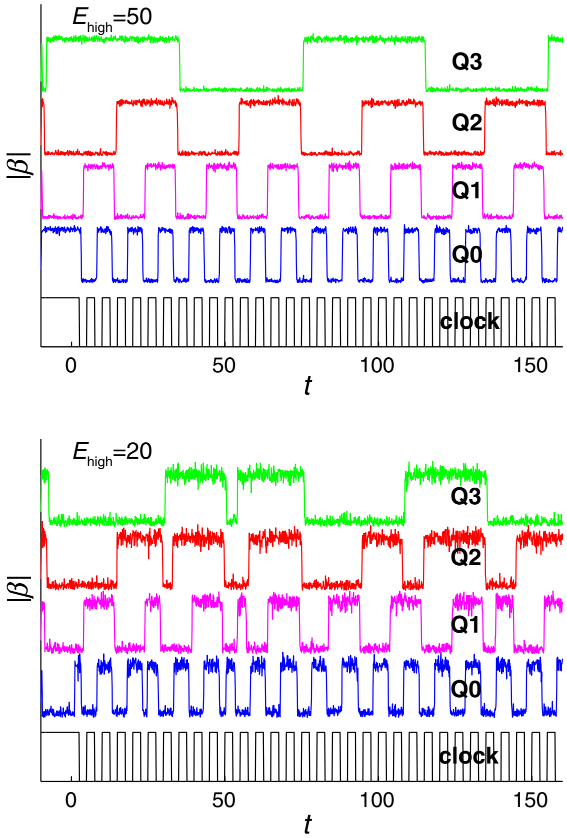

FIG. 13. Top: Simulated outputs of the four-bit ripple counter for $E_{\text{high}} = 50$. Bottom: Outputs for $E_{\text{high}} = 20$. The signals are averaged over a time interval of 0.1.

When flattened into its primitive components, this circuit contains 88 resonators, 240 beam splitters, and 176 phase shifters and requires 233 vacuum inputs and 72 nonvacuum inputs. The simulated behavior of the output fields is shown in Fig. 13. For $E_{\text{high}} = 50$, although the bit values start out with random values, the behavior for $t > 0$ is exactly as expected. However, for $E_{\text{high}} = 20$, random error events occur rather frequently. The estimated error rates for several values of E_{high} are plotted in Fig. 10. Since the counter circuit contains eight latches, we expect the error rate to be at least 8 times larger than the error rate for a single latch. The good agreement between the counter error rates and the red curve in Fig. 13 (which is 8 times the fitted latch error rate) suggests that spontaneous jumps in the latch circuits under the hold condition are the most important error source in the counter circuit.

It is also interesting to look at the Wigner functions of the resonators to see if the quantum noise grows as signals propagate through such a large circuit. The time-averaged Wigner functions for two selected resonators are shown in Fig. 14. One of the resonators is in the first flip-flop, and the other is in the last flip-flop. The small-scale quantum noise does not appear to grow. This is not surprising, considering the digital restoration properties demonstrated above for the basic gates. Of course, large errors associated with quantum

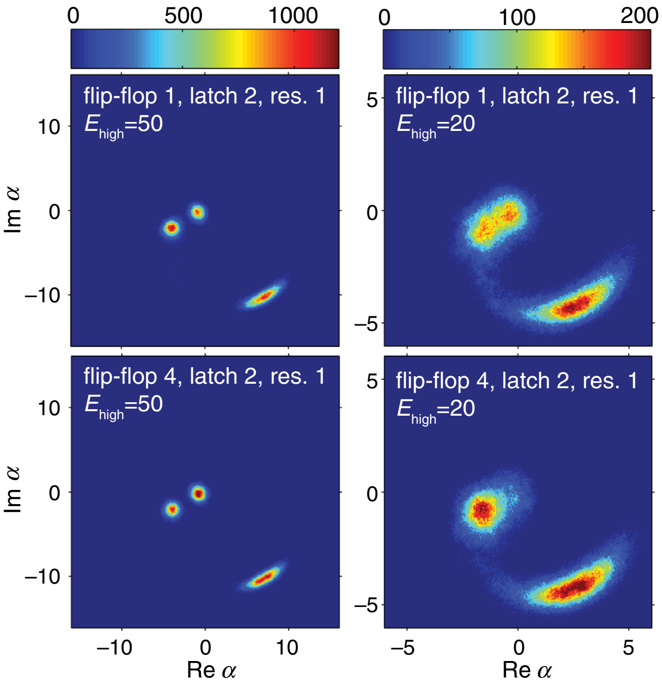

FIG. 14. For the four-bit ripple counter, the time-averaged Wigner functions of the first resonator in the second latch of flip-flop 1 (upper left) and flip-flop 4 (lower left) for $E_{\mathrm{high}} = 50$ and the same for $E_{\mathrm{high}} = 20$ (upper right and lower right).

jumps between bistable states of a gate will propagate through the system, and we expect the overall error rate to scale linearly with the number of components.

IV. OUTLOOK

We have demonstrated a simulation approach suitable for studying quantum noise in large-scale, nonlinear photonic circuits. We used this model to simulate a digital counter incorporating gates and latches based on previous designs. The results obtained so far suggest that the errors in the large-scale circuit are dominated by spontaneous jumps in the individual latches. From the error rates, we extrapolate that in the current design, the resonators within the latch circuit must contain approximately 180 photons in their on state to achieve acceptable error rates for computing.

The circuits shown above are built from a very limited set of existing designs chosen mainly to demonstrate the capabilities of this simulation approach. We are currently optimizing the circuits to make them more experimentally realizable. Initial results indicate that the number of resonators can be greatly reduced by factors as large as 5, in some cases. At the same time, we are working to make the circuits sufficiently tunable (by adjusting the amplitudes and phases of external inputs) to accommodate random variations in phases, resonant frequencies, and coupling strengths associated with fabrication imperfections.

At the same time, we are working to increase the capabilities of our model. We have recently incorporated the semiclassical equations used here into the QHDL software framework [13], which will allow a single tool to perform both semiclassical and full-quantum simulations for a given circuit and also allows for graphical construction of circuits. We are also working to expand the model to include quantum noise associated with other kinds of nonlinearities. Carrier-based nonlinearities are of particular interest for experiments. While the Kerr model is the simplest, requiring a single degree of freedom per resonator in our circuits, we find that the general design principles we apply to constructing the logic gates based on a Kerr nonlinearity fully translate to any sufficiently strong optical nonlinearity be it absorptive or dispersive.

ACKNOWLEDGMENTS

This work is supported by the Defense Advanced Research Projects Agency under Agreement No. N66001-12-2-4007.

[1] D. A. B. Miller, Are optical transistors the logical next step?, Nat. Photonics **4**, 3 (2010).

[2] T. Tanabe, M. Notomi, S. Mitsugi, A. Shinya, and E. Kuramochi, All-optical switches on a silicon chip realized using photonic crystal nanocavities, Appl. Phys. Lett. **87**, 151112 (2005).

[3] K. Nozaki, T. Tanabe, A. Shinya, S. Matsuo, T. Sato, H. Taniyama, and M. Notomi, Sub-femtojoule all-optical switching using a photonic-crystal nanocavity, Nat. Photonics **4**, 477 (2010).

[4] K. Nozaki, A. Shinya, S. Matsuo, Y. Suzaki, T. Segawa, T. Sato, Y. Kawaguchi, R. Takahashi, and M. Notomi, Ultralow-power all-optical RAM based on nanocavities, Nat. Photonics **6**, 248 (2012).

[5] J. S. Pelc, K. Rivoire, S. Vo, C. Santori, D. A. Fattal, and R. G. Beausoleil, Picosecond all-optical switching in hydrogenated amorphous silicon microring resonators, Opt. Express **22**, 3797 (2014).

[6] D. Ballarini, M. De Giorgi, E. Cancellieri, R. Houdré, E. Giacobino, R. Cingolani, A. Bramati, G. Gigli, and Daniele Sanvitto, All-optical polariton transistor, Nat. Commun. **4**, 1778 (2013).

[7] A. Faraon, I. Fushman, D. Englund, N. Stoltz, and J. Vuckovic Pierre Petroff, Coherent generation of non-classical light on a chip via photon-induced tunnelling and blockade, Nat. Phys. **4**, 859 (2008).

[8] R. Bose, D. Sridharan, H. Kim, G. S. Solomon, and Edo Waks, Low-photon-number optical switching with a single quantum dot coupled to a photonic crystal cavity, Phys. Rev. Lett. **108**, 227402 (2012).

[9] W. Chen, K. M. Beck, R. Bücker, M. Gullans, M. D. Lukin, H. Tanji-Suzuki, and V. Vuletić, All-optical switch and transistor gated by one stored photon, Science **341**, 768 (2013).

[10] Y.-D. Kwon, M. A. Armen, and H. Mabuchi, Femtojoule-scale all-optical latching and modulation via cavity nonlinear optics, Phys. Rev. Lett. **111**, 203002 (2013).

[11] J. Kerckhoff, M. A. Armen, and H. Mabuchi, Remnants of semiclassical bistability in the few-photon regime of cavity QED, Opt. Express **19**, 24468 (2011).

[12] J. Gough and M. R. James, The series product and its application to quantum feedforward and feedback networks, IEEE Trans. Autom. Control **54**, 2530 (2009).

[13] N. Tezak, A. Niederberger, D. S. Pavlichin, G. Sarma, and H. Mabuchi, Specification of photonic circuits using quantum hardware description language, Phil. Trans. R. Soc. A **370**, 5270 (2012).

[14] L. Bouten, R. van Handel, and A. Silberfarb, Approximation and limit theorems for quantum stochastic models with unbounded coefficients, J. Funct. Anal. **254**, 3123 (2008).

[15] H. Mabuchi, Derivation of Maxwell-Bloch-type equations by projection of quantum models, Phys. Rev. A **78**, 015801 (2008).

[16] A. E. B. Nielsen, A. S. Hopkins, and H. Mabuchi, Quantum filter reduction for measurement-feedback control via unsupervised manifold learning, New J. Phys. **11**, 105043 (2009).

[17] S. J. Carter, Quantum theory of nonlinear fiber optics: Phase-space representations, Phys. Rev. A **51**, 3274 (1995).

[18] H. A. Haus and W. Huang, Coupled-mode theory, Proc. IEEE **79**, 1505 (1991).

[19] C. Gardiner and P. Zoller, *Quantum Noise: A Handbook of Markovian and Non-Markovian Quantum Stochastic Methods with Applications to Quantum Optics*, Springer Series in Synergetics (Springer, New York, 2004).

[20] M. O. Scully and M. S. Zubairy, *Quantum Optics* (Cambridge University Press, Cambridge, England, 1997).

[21] C. W. Gardiner and M. J. Collett, Input and output in damped quantum systems: Quantum stochastic differential equations and the master equation, Phys. Rev. A **31**, 3761 (1985).

[22] C. W. Gardiner, A. S. Parkins, and P. Zoller, Wave-function quantum stochastic differential equations and quantum-jump simulation methods, Phys. Rev. A **46**, 4363 (1992).

[23] K. Huybrechts, G. Morthier, and B. Maes, Symmetry breaking in networks of nonlinear cavities, J. Opt. Soc. Am. B **27**, 708 (2010).

[24] S. M. Tan, A computational toolbox for quantum and atomic optics, J. Opt. B **1**, 424 (1999).

[25] For these higher photon numbers, the QOT function mcsolve had to be recompiled for double-precision arithmetic to give accurate results.

[26] H. Mabuchi, Nonlinear interferometry approach to photonic sequential logic, Appl. Phys. Lett. **99**, 153103 (2011).

[27] P. Horowitz, W. Hill, and T. C. Hayes, *The Art of Electronics* (Cambridge University Press Cambridge, England, 1989).